



Realize larger grain size of $\text{CH}_3\text{NH}_3\text{PbI}_3$ film with reduced non-radiative recombination for high performance perovskite solar cells via precursor colloidal size engineering

Yan Li^{a,*}, Jialu Zheng^a, Xuelian Chen^a, Can Sun^a, Hao Jiang^a, Guangrong Li^b, Xiaoyong Zhang^{a,*}

^a School of Materials Science and Engineering, Xi'an Shiyou University, Xi'an 710065, China

^b State Key Laboratory for Mechanical Behavior of Materials, School of Materials Science and Engineering, Xi'an Jiaotong University, Xi'an, Shaanxi 710049, China



ARTICLE INFO

Article history:

Received 17 April 2021

Received in revised form 4 July 2021

Accepted 22 July 2021

Available online 27 July 2021

Keywords:

Methylammonium lead iodide ($\text{CH}_3\text{NH}_3\text{PbI}_3$)

Perovskite solar cells

$\text{CH}_3\text{NH}_3\text{I}$ purification

Grain size

Grain boundary defect

ABSTRACT

In $\text{CH}_3\text{NH}_3\text{PbI}_3$ perovskite solar cells, enhancement grain size of $\text{CH}_3\text{NH}_3\text{PbI}_3$ to reduce the non-radiative at grain boundaries is an important way to reach high performance perovskite solar cell. However, it is still a challenge to enhance the grain size of $\text{CH}_3\text{NH}_3\text{PbI}_3$ through a simple and low cost way. In this work, a larger precursor colloidal size is realized through tuning morphology of precursor $\text{CH}_3\text{NH}_3\text{I}$ using a polar solvent of ethanol during purification, yielding a larger grain size of $\text{CH}_3\text{NH}_3\text{PbI}_3$ film, and the as-prepared perovskite solar cells are shown to be dramatically increased to 17.49% with an increase in short circuit density, fill factor and open circuit voltage, as compared to that (14.28%) in the control device with $\text{CH}_3\text{NH}_3\text{I}$ purified by non-polar solvent of diethyl ether. The investigation result showed the increased efficiency of perovskite solar cells prepared by ethanol purification is ascribed to a faster charge transfer at $\text{CH}_3\text{NH}_3\text{PbI}_3/\text{TiO}_2$ interface resulting from the reduced grain boundary defects. Our work provides a route for improving the $\text{CH}_3\text{NH}_3\text{PbI}_3$ device efficiency through a simple yet effective approach.

© 2021 Published by Elsevier B.V.

1. Introduction

Today, power conversion efficiencies (PCEs) of the hybrid perovskite solar cells (PSCs) have exceeded 25%, and the maximum module areas have reached 808 cm^2 . The rapid progress makes the hybrid PSCs potentially appealing for fabrication of future photovoltaics among other types of photo-absorbers. So far, greening of precursor solution, high throughput production technology, high environment stability and fabrication high quality perovskite film are all the directions for its commercialization.

The high quality perovskite film requires reduced non-radiative recombination during the charge transport processes. The non-radiative recombination via defects at the grain boundaries is mainly focused, which are strongly linked with the composition, crystallinity and morphology of the perovskite film. The non-radiative recombination will unavoidably influence photogeneration, conversion and losses of charge carrier in perovskite film, and it will ultimately affect performances of the PSCs [1–3]. Many strategies have been proposed to effectively reduce the loss of these charge

carriers that are recombined at the grain boundary [4]. For example, by adding small molecule in the precursor solution to passivate the defects in perovskite film [5–7], and to optimal the preparation method of TiO_2 electron transport layer (CTL) to suppress defect recombination while promote interface charge transfer at the interface [8]. In addition to the aforementioned engineering methods, though optimization of crystal growth and morphology control to realize $\text{CH}_3\text{NH}_3\text{PbI}_3$ (MAPbI_3) film with large grain size are also successful in reducing recombination loss [9,10]. Xiao et al. successfully increased the size of MAPbI_3 grains with improved crystallinity via a post-treatment procedure using solvent annealing, and they found that this method was effective in improving overall performances of the MAPbI_3 PSCs [11]. However, the thermal treatment process may induce the decomposing the perovskite film [12–14]. To get the perovskite film with large grain size without thermal treatment, solution engineering is another low cost way. Lee et al. showed that crystal growth and morphology of MAPbI_3 can be easily controlled owing to a weak chemical interaction in the adduct that are formed as a result of chemical reaction between PbI_2 and a polar aprotic solvent (oxygen-donor N, N'-dimethyl sulfoxide) that dissolves it [15]. According to the LaMer model, solution processing of the MAPbI_3 crystals are often divided into three stages, which are supersaturation of precursors, nucleation and growth up [16,17].

* Corresponding authors.

E-mail addresses: li1988yan@163.com (Y. Li), xyzhang@xsyu.edu.cn (X. Zhang).

Yang et al. demonstrates that the number of nucleation sites, which are tuned by chamber pressure during drying of MAPbI₃, and plays a critical role in achieving a full coverage of MAPbI₃ film on substrates as well as to prolong carrier lifetime in MAPbI₃ [18]. Bi et al. reported that desirable MAPbI₃ with large grains, which has a high average aspect ratio of 2.3–7.9, are achieved with less grain boundary defects via MAPbI₃ growth control using non-wetting underlayer. In comparison, non-wetting substrates suppress heterogeneous nucleation and facilitate grain boundary migration in MAPbI₃ with less dragging force during MAPbI₃ crystal growth. As a result, MAPbI₃ with large grains and improved crystallinity dramatically reduce charge recombination, which is comparable with single crystal MAPbI₃ [19].

Further, Yan et al. revealed that the MAPbI₃ precursor solution is actually consisting of colloidal dispersions in a precursor solution rather than a single-phase solution [20]. They also pointed out that organic solvent with a polar nature is advantageous in opening the layered skeleton of PbX₂ to form the [PbX₆]⁴⁻ soft template, so that the MAPbI₃ precursor solution are stabilized with polar solvent when MA⁺ incorporate [PbX₆]⁴⁻ through electrostatic attraction. During nucleation, in particular, the nature of the precursor solution, meaning the solute coordination interaction, the precursor dissolution and recrystallization as well as the electrostatic attraction and self-assembly of charged unit etc., strongly impact by the nucleation rate, the number of nucleates and crystallization kinetics of the MAPbI₃ precursor [21–23]. The grain size of MAPbI₃ is strongly depending on the chemistry nature of the MAPbI₃ colloidal precursor solution [24–26]. Meng et al. also shows that the size of NH₂CH₃NH₂PbI₃ (FAPbI₃) colloids is reduced by introducing a non-aprotic formic acid (HCOOH) into the precursor solution, leading to a more uniform FAPbI₃ film [27]. Besides, Li et al. demonstrates that a grain size (~ 3 μm) in MAPbI₃ is achieved via manipulation of the size of MAPbI₃ colloidal crystals with introduction of MAI prior to thermal treatment [28]. Therefore, the chemistry nature of MAPbI₃ colloidal precursor indeed plays an important role in determining the grain size of MAPbI₃ film. Unfortunately, so far seldom researches have been focusing on controlling of MAPbI₃ colloidal size for a high-performance MAPbI₃ PSCs without additional additives. Consequently, a simpler yet effective method is urgently needed to further increase MAPbI₃ grains with less defects at grain boundaries.

In this work, we first study nucleation and crystallization of MAPbI₃ colloids using solution processing as well as the underlying mechanisms for growth of large grains in MAPbI₃. Next, we investigate the influence of grain boundaries in MAPbI₃, where defects are anticipated to exist, on non-radiative recombination at the MAPbI₃/electron transport layer (ETL) depending on the interface charge transfer. In particular, the MAPbI₃ PSCs that are purified with an aprotic solvent prior to nucleation of MAPbI₃ colloids have shown a higher efficiency of 17.49%, as compared to the control device (14.28%). Last but not least, we demonstrate that the large MAPbI₃ grains that are originated from the small and size-uniform precipitates of CH₃NH₃I (MAI) provide a new route for fabrication of highly efficient hybrid MAPbI₃ PSCs without additional additives for the future.

2. Experimental section

2.1. Preparations of MAI powder and MAPbI₃ solution

All purchased chemicals were used without purification. First, the methylamine solution (CH₃NH₂, 33 wt% in ethanol, Sigma-Aldrich) was added dropwise into the hydroiodic acid (HI, 57 wt% in water, Sigma-Aldrich) under stirring. When it reached an equal molar mass to HI, the mixed solution was stirred for 2 h (0 °C, ambient air) to allow complete reaction to MAI. Next, the precipitation of MAI was undertaken in a rotary evaporator (50 °C, 0.1 MPa), resulting in white MAI powder. Afterwards, the MAI powder was

purified by two solvents separately for 30 min, which is necessary to separate the MAI powers from unreacted chemicals. Both solvents were ethanol (C₂H₅OH or EtOH, 99.0%, Sigma-Aldrich) and diethyl ether (C₄H₁₀O or Et₂O, 99.5%, Sigma-Aldrich). The MAI precipitates using EtOH and Et₂O thus referred as EtOH-MAI and Et₂O-MAI, respectively. The purification processes were repeated three times to ensure that unreacted residues are completely removed from the EtOH-MAI and Et₂O-MAI powders.

To obtain MAPbI₃ solution, lead iodide (PbI₂, 99.9%, Xi'an Polymer Light Technology Corp.) and the aforementioned MAI powders were stoichiometrically dissolved (35 wt% in concentration) in a mixed solution, which was composed of γ -butyrolactone (99%, Sigma-Aldrich) and dimethylsulfoxide (99%, Sigma-Aldrich) solvents (7:3, vol:vol), and then stirred for 5 h (70 °C, ambient air). Subsequently, the MAPbI₃ solutions were successfully obtained with EtOH-MAPbI₃ and Et₂O-MAPbI₃ referring to the different MAPbI₃ colloids, where the MAI were purified by EtOH and Et₂O, respectively.

2.2. Preparation of MAPbI₃ films

Before spin-coating to achieve MAPbI₃ layers, FTO substrates (FTO, TEC-15, LOF) were firstly treated in consecutive ultra-sonic baths using acetone and isopropanol; 5 min each. Next, the substrates were tried with a nitrogen flow. Secondly, MAPbI₃ layers was spin-coated (4000 rpm, 10 s) in ambient air, followed by a rapid drying process under a low vacuum (1000 Pa) assisted procedure, which we referred to as “gas pumping” method and was demonstrated to be particularly beneficial for growth of MAPbI₃ grains by Yang et al. [29,30]. All of these procedures were carried out at room temperature (25 °C). Accordingly, EtOH-MAPbI₃ and Et₂O-MAPbI₃ films were obtained depending on the purification solvents during MAI precipitation as aforementioned.

2.3. Fabrication of MAPbI₃ PSCs

First, TiO₂ compact layer was spin coated (3000 rpm, 6 s) on the FTO substrates and thermally treated at 450 °C for 30 min. Next, EtOH-MAPbI₃ and Et₂O-MAPbI₃ were deposited separately as described in Section 2.2 and they were also thermally treated at 100 °C for 30 min. For hole transport layer, the hole transport material (HTM) solution was spin coated (3000 rpm, 30 s), where HTM solution consists of 2, 2', 7, 7' - tetrakis(N,N-di-*p*-methoxyphenylamine) - 9, 9' - spirobifluorene (Spiro-OMeTAD) (80 mg), 4-tert-butylpyridine (28.5 μl) and (17.5 μl) of Lithium-bis(trifluoromethanesulfonyl)imide (Li-TFSI) solution (520 mg Li-TFSI in 1 ml acetonitrile) and chlorobenzene (1 ml). All the necessary chemicals for preparation of the Spiro-OMeTAD solution were purchased from Xi'an Polymer Light Technology Corp. China. Last, a silver layer (200 nm) was thermally evaporated, so that the MAPbI₃ PSCs were successfully fabricated with EtOH-MAPbI₃ and Et₂O-MAPbI₃ photoactive layers, coded as EtOH PSCs and Et₂O PSCs respectively.

2.4. Characterizations

The size of the MAPbI₃ colloids was measured by dynamic light scattering (DLS) using Brookhaven 90Plus particle size analyzer. The contact angle of the MAPbI₃ solutions was determined by surface tension meter (SDT, KRUSS, Germany) on silicon substrates.

For MAI powders and MAPbI₃ films, surface morphologies were monitored using a field emission scanning electron microscopy (FESEM, TESCAN, Czech Republic) and an atomic force microscopy (AFM, Innova, America). X-ray diffraction (XRD) patterns were obtained using an X-ray diffractometer (D8 Advance, Germany) with Cu K_α radiation. For MAPbI₃ films, the absorption spectra were measured using a UV-VIS spectrophotometer (U-4100, Hitachi, Japan).

The steady-state photoluminescence (PL) spectra were performed by spectrophotometer (Fluoromax-4, Horiba Jobin Yvon, France) with excitation of mono-wavelength at 560 nm. The time-resolved photoluminescence (TRPL) spectra of the MAPbI₃/TiO₂ junctions were measured by a labRAM HR800 setup (Horiba Jobin Yvon, France) with a 400 nm light pulse from a HORIBA Scientific DeltaPro fluorimeter.

For MAPbI₃ devices, the current density- voltage (*J*-*V*) curves were measured by a solar simulator (Oriel 94023A, Newport) with light intensity of 100 mW cm⁻² and equipped with a Keithley 2400 digital source meter (-0.2–1.3 V). Before measurement, the light intensity was calibrated with a reference device using a single-crystal silicon photovoltaic device (91150V, Oriel Instruments). The active area of the PSC devices was controlled to 0.10 cm² using a metal mask. Electrochemical impedance spectroscopy (EIS) spectra were carried out using an electrochemical workstation (IM6, ZAHNER, Germany) at the bias condition (-*V*_{OC}) with an AC probing signal (amplitude 20 mV, frequency range 10⁻¹ to 10⁶ Hz) without shielding.

3. Results and discussions

After precipitation of MAI using rotary evaporation, the MAI precipitates were repeatedly purified by procedures of dissolution and precipitation, which is necessary, so that unfavorable chemicals that are unreacted at an earlier stage are removed from MAI. Herein, to increase the grain size of perovskite film, the commonly used

aprotic and non-aprotic solvents of EtOH and Et₂O were acted as such purification solvents. The basis for the selection can be concluded as: during the dissolution process, EtOH has a larger molecular polarity than that in Et₂O, which subsequently enhances dissolution of polar MAI in polar EtOH; During the precipitation process, the latent heat of evaporation, which measures the minimum required energy for evaporation of an organic solvent of a certain mass, in EtOH (840 kJ/kg) is two times higher than that in Et₂O (350 kJ/kg), and then the nucleation and crystallization will be restrained for the evaporation of EtOH because of the a larger amount of absorption of heat compared with Et₂O.

Indeed, the differ purification procedures result in different microstructures in the Et₂O-MAI and EtOH-MAI precipitates, shown in Fig. 1(a) and (b), respectively. From the images, EtOH-MAI precipitates are rather small and are scattered in size (Fig. 1(a)). By contrast, Et₂O-MAI precipitates are relatively larger and appear to be smooth and continuous in surface morphology (Fig. 1(b)). The photographic images of both powders are shown in Fig. S1(a) and (b). The EtOH-MAI powder is shown to have different crystallographic planes for the different intensity ratios in comparison with Et₂O-MAI (Fig. S1(c)). However, further assignment of each peak with Miller index is challenging, owing to lack of standard Powder Diffraction (PDF) card for MAI. The reason of the contrast in MAI surface morphologies using different purification solvents is anticipated to be correlated with the polarity of the organic solvents [20].

Under surface SEM images, both MAPbI₃ films are uniform and fully covered on the surface of TiO₂ ETL (Fig. 1(e) and (f)). The EtOH-

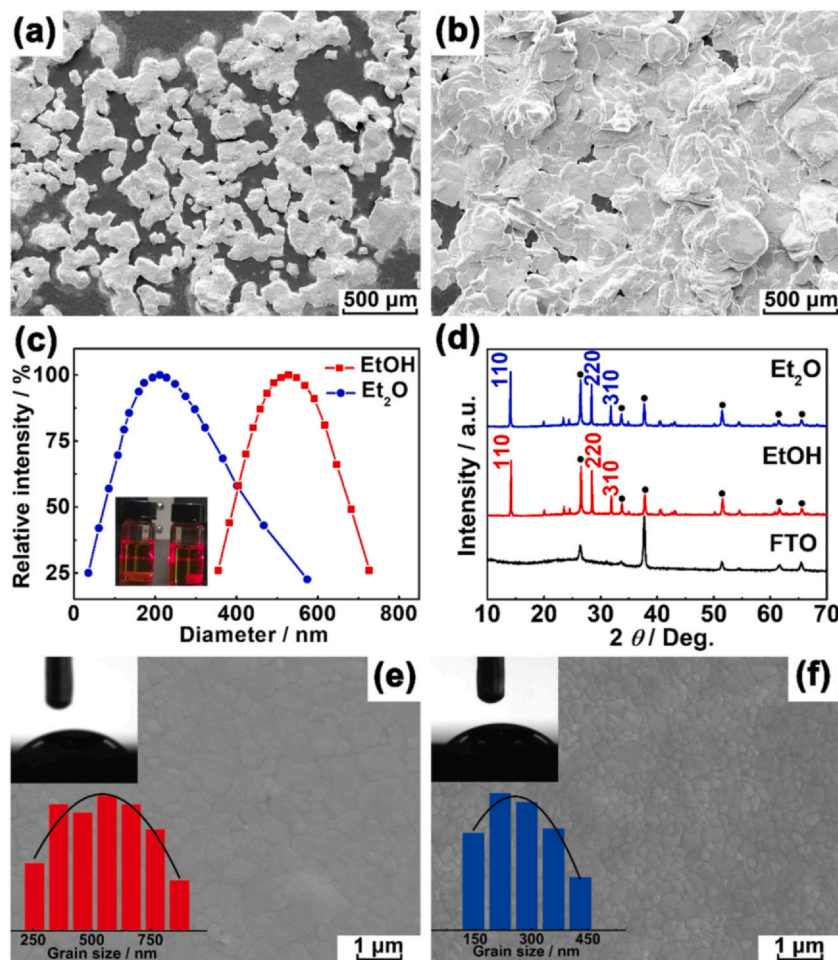


Fig. 1. SEM images of MAI powders prepared with (a) EtOH and (b) Et₂O. (c) Size distributions of the two MAPbI₃ colloid solutions determined by DLS. The inset shows photographs of the MAPbI₃ colloidal precursor solutions. (d) XRD patterns of the two samples. Surface microstructures of (e) EtOH-MAPbI₃ and (f) Et₂O-MAPbI₃ with grain size distribution. The inset also shows the contact angle of the purifying agents of EtOH and Et₂O on a silicon wafer.

MAPbI₃ layer shows larger surface grain diameters (range of 250–750 nm, median value of 600 nm) than that those in the Et₂O-MAPbI₃ (range of 150–450 nm, median value of 300 nm). However, irrespective of purifying solvents, both MAPbI₃ exhibits the tetragonal perovskite with diffraction peaks of (110), (220) and (310), observed from the XRD patterns (Fig. 1d). However, {110} peaks accounts as much in EtOH-MAPbI₃ (82.5%) as in Et₂O-MAPbI₃ (82.2%) (Table S1). That means the crystallinity stay unchanged in both samples even if EtOH-MAI has a larger grain size than Et₂O-MAI.

Previous results showed the difference microstructures of MAPbI₃ layers was strongly relied on the wetting properties between the precursor solution and the substrates [18]. In order to confirm that the size discrepancy of the surface microstructures of the two MAPbI₃ films were affected by the precursor solutions themselves rather than the wetting properties between the substrate and precursor solution, the wetting properties of the two MAPbI₃ solutions are examined on the same silicon wafer (Si). The results show that both solutions have a contact angle of 43° (inset of Fig. 1(e) and (f) as well as Fig. S2 for other locations of the silicon wafer for accuracy), which indicates that the precursor solutions themselves, indicating the colloidal states, would play a major role in surface grain size of MAPbI₃ layer rather than the interface between the substrate and precursor solution.

The colloids size of the MAPbI₃ precursor solution from EtOH and Et₂O purified MAI precipitates are determined using DLS. As it can be seen in Fig. 1(c), the size of Et₂O-MAPbI₃ colloids are widely spanned in the range of 0–600 nm with a median value of approximately 200 nm. Whereas, the size of EtOH-MAPbI₃ colloids are concentrated in the range of 400–700 nm with median value of 600 nm. Based on the research results published by Espiau de Lamaestre et al. [31], during the preparation process of the MAPbI₃ film, the continuous evaporation results in an inhomogeneous system for the nucleation and growth up, and the final size distribution should be apparently log-normal distribution, therefore the log-normal distribution of the grain size for both films has been added in Fig. S3. However, based on Fig. S3, there is almost the same deviation change tendency between the normal distribution and log-normal distribution for both films, which illustrates there is dynamic equilibrium between screening length (λ) and the implanted profile width (Δ), where λ describes the concentration field interaction of neighboring precursor colloidal, and Δ is equivalent to the diffusion distance caused by concentration difference in crystallization process of MAPbI₃ film. The above results prove that the “gas pumping” method for preparing both of the EtOH-MAPbI₃ film and Et₂O-MAPbI₃ film is a fast mass transfer process, and the main difference is attributed to the larger colloidal size of the EtOH-MAPbI₃ precursor compared with

Et₂O-MAPbI₃ precursor. The dependence of colloid size of MAPbI₃ on purifying solvents suggests that the morphology of MAI powder probably has a strong influence on nucleation and growth of MAPbI₃ colloids. That is to say, smaller size of precipitates in EtOH-MAI with larger surface area are likely to induce a rapid dissolution during reaction, which facilitates a rapid movement of MA⁺ to be incorporated by the [PbI₆]⁴⁻ octahedrons [20].

In order to further investigate the underlying mechanism of the contrast in grain size due to the size of MAPbI₃ colloids, we turn to the fundamental theories of the crystallization process of MAPbI₃ colloids, as depicted in Fig. 2(a) and (b). Typically, the low pressure preparation method for the perovskite film provides the same supersaturation level of the precursor solution, yielding the same number of the nuclei in the solution at the original, and the large EtOH-MAPbI₃ colloid size is expected to rapidly reduce the driving force of supersaturation state, as it shows large pieces of stacking, resulting a large grain size of the film (Fig. 2(b)) [19]. By contrast, smaller colloid size of Et₂O-MAPbI₃ are expected to be insufficient to reduce the driving force of supersaturation state, as it shows small pieces of stacking, resulting more nuclei appear in the growth up process, therefore a small grain size of the film is reached (Fig. 2(a)). The AFM measurements have been down and shown in Fig. S4 in the Supporting information. As can be seen, the EtOH-MAPbI₃ film shows the larger grain size compared with the Et₂O-MAPbI₃ film, which is consistent with the SEM results. The cross sectional view of both films are shown in Fig. S5.

The planar structure and the band diagram of MAPbI₃ devices is displayed in Fig. 3(a). The maximum *J-V* curves of both EtOH-MAPbI₃ PSC and Et₂O-MAPbI₃ PSC are shown in Fig. 3(b), and the champion of EtOH-MAPbI₃ PSC exhibit the short circuit density (J_{SC}) of 22.96 mA cm⁻², open circuit voltage (V_{OC}) of 1.00 V, fill factor (FF) of 76.41 and power conversion efficiency (PCE) of 17.49%. All of the four parameters of the highest performance of EtOH-MAPbI₃ PSC are higher than the highest performance of Et₂O-MAPbI₃ PSC. After 14 more devices are characterized, there are also a clearly improvement in the PCEs of the EtOH-MAPbI₃ PSCs (Figs. S6 and S7 and Table S2) in comparison with that the device based on Et₂O-MAPbI₃ film (Figs. S6 and S7 and Table S3), and the increase of the PCEs can be mainly attributed to the improvement of the J_{SC} for the V_{OC} being almost comparable of both solar cells (Fig. S7). It also can be seen, the discrete distributions of *J-V* parameters of the EtOH-MAPbI₃ PSCs are obviously restrained in comparison with Et₂O-MAPbI₃ PSCs. Both of the EtOH-MAPbI₃ PSCs and Et₂O-MAPbI₃ PSCs have the stabilized current density at the maximum output power point (Fig. S8) over a period of 10 min, which illustrate the performance of both PSCs are stable under continuous illumination.

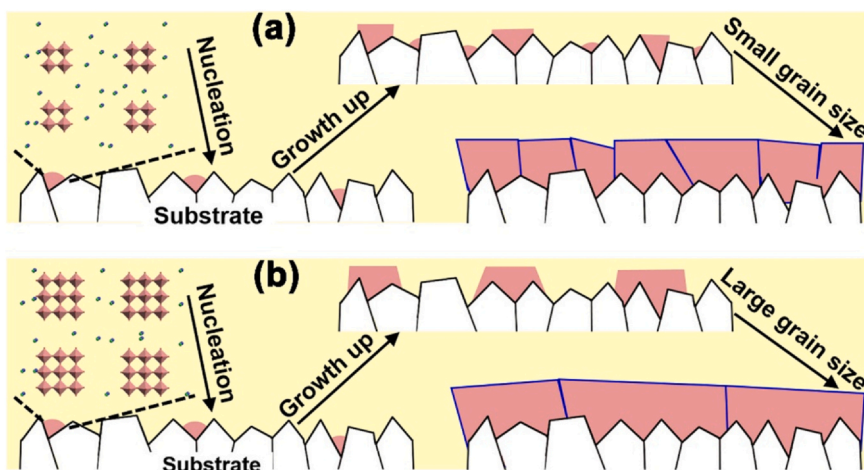


Fig. 2. Schematic of nucleation and growth process of MAPbI₃ (a) with small grain size and (b) with larger grain size.

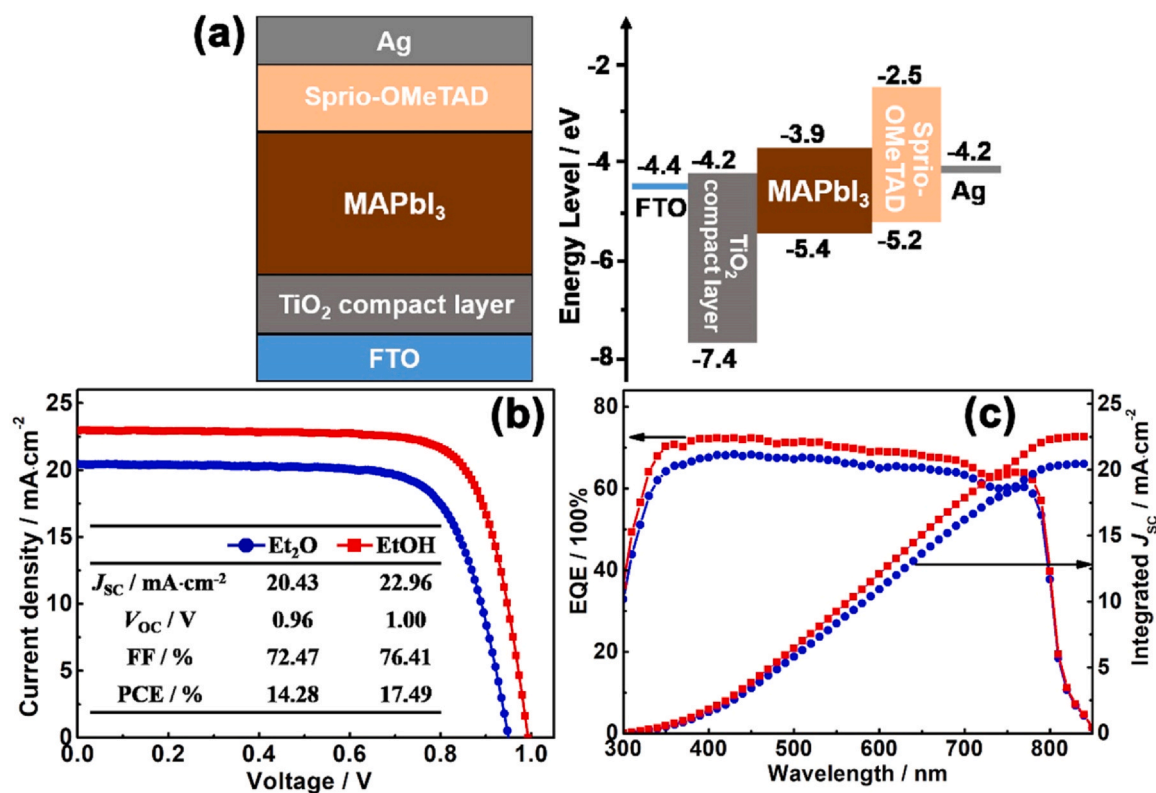


Fig. 3. (a) Schematic of MAPbI₃ device structure and its band diagram. (b) $J-V$ curves and (c) EQE spectra with integrated current densities for EtOH- MAPbI₃ and Et₂O- MAPbI₃ PSCs.

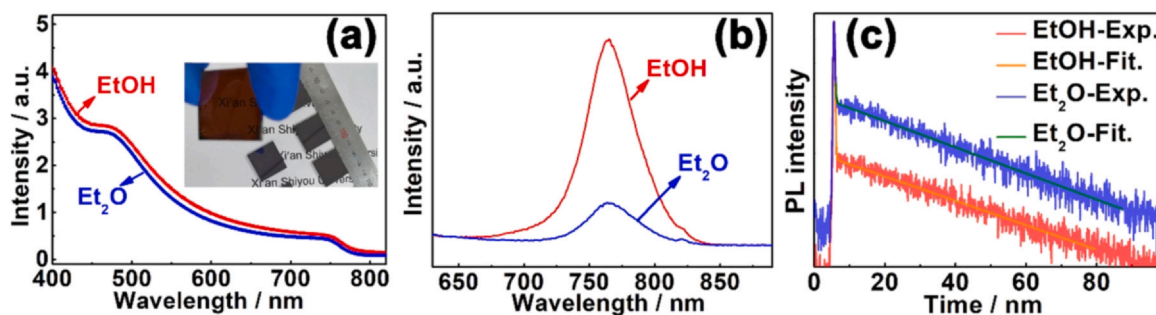


Fig. 4. (a) Absorption spectra and (b) steady-state PL spectroscopy measurements of EtOH-MAPbI₃ and Et₂O-MAPbI₃ layers. The inset in (a) shows a photograph of MAPbI₃ layer spin-coated on substrates ($2.5 \times 2.5 \text{ cm}^2$ in size). (c) Time-resolved PL spectra of EtOH-MAPbI₃/TiO₂ and Et₂O-MAPbI₃/TiO₂ interfaces.

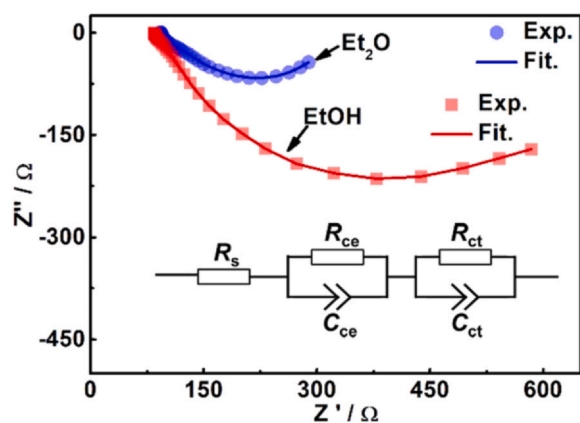


Fig. 5. Nyquist plots of EtOH-MAPbI₃ and Et₂O-MAPbI₃ PSCs measured at a reverse bias (amplitude of V_{OC}).

To investigate the reasons of the increase of J_{SC} in EtOH-MAPbI₃ PSCs, the external quantum efficiency (EQE) of the champion solar cells in the wavelength range of 300–800 nm (Fig. 3(b)) were characterized. The integrated J_{SC} are 20.47 and 22.50 mA cm^{-2} , which correlate well with the J_{SC} (20.43 and 22.96 mA cm^{-2}) measured in the $J-V$ curves for Et₂O and EtOH devices, respectively. The EQE performance of EtOH-MAPbI₃ PSC is higher than Et₂O-MAPbI₃ PSC in the wavelength region of 300–800 nm, which can be attributed to the improvement of light absorption ability or the restrained charge transport and recombination behaviors. In addition, the EQE performance is obviously better in the short wavelength region (300–400 nm), which is mainly contributed by the collection of photoexcited charge carriers at the MAPbI₃/TiO₂ interface, rather than the rest of the location range. This suggests that interface non-radiative recombination is reduced owing to improved qualities of EtOH-MAPbI₃ films.

In order to further investigate the reason of an increase in J_{SC} in the EtOH-MAPbI₃ device in comparison with the Et₂O-MAPbI₃

Table 1

Lifetime components and recombination resistance extracted from time-resolved PL measurements and Nyquist plots, respectively.

	τ_1 / ns	τ_2 / ns	R_{ce} / Ω	R_{ct} / Ω
EtOH-MAPbI ₃	0.14	12.42	52.05	587.73
Et ₂ O-MAPbI ₃	0.15	68.08	44.12	144.81

device, we performed absorption spectra in the UV–VIS spectral range (Fig. 4(a)). As can be observed, though there is a slight increase in absorption (the range of 400–750 nm) in the EtOH-MAPbI₃ film, both films are comparable, therefore, the increase in J_{SC} in the EtOH-MAPbI₃ device can not be attributed to the absorption ability of the MAPbI₃ films. Furthermore, we performed PL on both samples (Fig. 4(b)). As can be seen, the PL intensity of the major peak that is located at 765 nm is strongly quenched in the Et₂O-MAPbI₃ in comparison with EtOH-MAPbI₃. The strong quenching in PL intensity is thus ascribed to the non-radiative recombination that is due to defects. Considering the strong body defect tolerance ability of the organic-inorganic hybrid perovskite films, the restrained quenching in PL intensity of the EtOH-MAPbI₃ can be attributed to the decrease of the grain boundary defects due to the large grain size of the EtOH-MAPbI₃ film. Next, we investigate charge transportation behavior of the MAPbI₃/TiO₂ film using TRPL measurement (Fig. 4(c)), and the results were fitted using a biexponential decay equation, so that two components in different time domains (τ_1 and τ_2) are extracted (Table 1). The TRPL intensities for the both interfaces are observed to first have a rapid decay (timescale of approximately 150 ps, Table 1), irrespective of the MAPbI₃ used. The TRPL then decays more slowly over the nanosecond timescale. For the slow decay, the EtOH-MAPbI₃/TiO₂ sample shows a faster decay time τ_2 of 12.42 ns, compared to 68.08 ns for the Et₂O-MAPbI₃/TiO₂ sample, which illustrate a faster charge transfer process of the EtOH-MAPbI₃/TiO₂ interface due to the restrained non-radiative recombination at the grain boundary. Furthermore the theory proposed by Wight et al. [32] has been used to explain the relationship between slow decay (τ_2) and grain size of both types of MAPbI₃ films. A simple Eq. (1) can be concluded based on their theory, where D is the diffusivity, and S is the recombination velocity of the grain boundary. Take the EtOH-MAPbI₃ film as a demonstration, based on Fig. 1 and Table 1, τ_2 is 12.42 ns, D can be estimate as 1.7 cm²/s [33], the median grain size value (W) is 600 nm, then based on Eq. (1), the recombination velocity (S) should be about 5.8×10^3 cm/s, and the D/W should be $\sim 2.8 \times 10^4$ cm/s. Therefore, $S < D/W$, and it should be a recombination-controlled process in the MAPbI₃ film, rather than a diffusion-controlled process. There is no significant depression of the carrier concentration, and the bulk and surface-controlled recombination processes are in parallel in the perovskite film region. Based on Wight et al. [32] theory, the lifetime of the steady-state and the transient-state for the recombination-limited case is the same, therefore the calculated results of the slow decay (τ_2) of the EtOH-MAPbI₃ layer is 10.34 ns (i.e. $W/S = 10.34$ ns, where W is 600 nm and S is 5.8×10^3 cm/s). The calculated result is comparable to the measurement result by TRPL. It can be concluded though enlarge the grain size of EtOH-MAPbI₃ film, both the bulk and surface-controlled recombination are restrained, therefore, it results in an enhanced PL and a faster charge transfer process (i.e. decreased τ_2) of the EtOH-MAPbI₃/TiO₂ interface due to the restrained non-radiative recombination at the grain boundary.

$$\tau_2 = W^2/D + W/S \quad (1)$$

We also performed electrochemical impedance spectroscopy (EIS) measurements with Nyquist plots displayed for both PSC devices (Fig. 5) to investigate the influence of grain boundary defects to the charge transfer at MAPbI₃/TiO₂ interface. We used a simplified

transmission line model to describe the Nyquist plots for the two junctions, where R_{ce} and C_{ce} are resistance and capacitance at the counter electrode, and R_{ct} and C_{ct} are the charge recombination resistance and capacitance of the MAPbI₃/TiO₂ interfaces [34,35]. In particular, R_{ct} and R_{ce} correspond to the semi-circle in the Nyquist plots from right (the low frequency region) to left (the high frequency region, too small to be identified in Fig. 5), respectively. By fitting the Nyquist plots, the important parameters can be extracted (Table 1). As we are more interested in the MAPbI₃/TiO₂ interface charge transfer of the MAPbI₃ device, in this work we have performed the EIS studies of the devices at external reverse bias condition ($-V_{OC}$), so that the actual space charge region is strongly localized at the MAPbI₃/TiO₂ interface. Because the external bias could also alter the probing region during EIS. As can be seen, EtOH-MAPbI₃ PSC has a larger R_{ct} (587.73 Ω) than that (144.81 Ω) in the Et₂O-MAPbI₃ PSC, indicating suppressed recombination at the MAPbI₃/TiO₂ interface with EtOH purified MAI, compared to Et₂O purified MAI (Table 1).

More importantly, we note that the results that are achieved in this work might provide a new route that is simple yet effective to enhance grain size of perovskite film for reducing non-radiative defect recombination for future energy conversion and storage devices on a broader scope. Purification of MAI using an aprotic solvent ethanol will certainly be advantageous for synthesis of tandem and hybrid perovskite for electrolysis cells, as well as enriching the overall performances of the renewable solar fuel. In addition, to meet the growing demand of energy for the future, systems that integrate both energy conversion and storage parts such as solar cells using different materials e.g., silicon, Cu(In,Ga)(Sn,Se)₂, polymers, dye molecules as well as perovskite and lithium-ion battery, nanogenerator, supercapacitor, photoelectrosynthetic cell and electrolysis cell will be urgently needed. Therefore, reducing defect recombination in the materials and systems is urgently needed in these self-powered systems which are featured to be small, lightweight, highly packed and reliable.

4. Conclusions

In summary, we demonstrate that purification of MAI with the solution of different polarity prior to the reaction of MAI and PbI₂ can effectively change the columnar grain size of MAPbI₃ films. The result show the EtOH-MAPbI₃ has a larger columnar grain size (median value of 500 nm) with less defect containing grain boundaries compared with the Et₂O-MAPbI₃ (median value of 300 nm). The underlying cause is the increased colloidal size of EtOH-MAPbI₃ compared with Et₂O-MAPbI₃. The PCE of MAPbI₃ PSC device is increased from 14.28% to 17.49% with an increase of J_{SC} , FF and V_{OC} with MAI purified by an aprotic solvent (EtOH). The increasing of J_{SC} is strongly influenced by an improved absorption in EtOH-MAPbI₃ layer and the restrained non-radiation recombination. A strong defect recombination in Et₂O-MAPbI₃ is further clarified with a strong quenching in photoluminescence as compared to that in EtOH-MAPbI₃. In addition, Et₂O-MAPbI₃/TiO₂ is shown to have a slow interface charge transfer reflected EtOH-MAPbI₃/TiO₂ due to a slower TRPL live time and small resistance.

CRedit authorship contribution statement

Yan Li: Conceptualization, Methodology, Writing – original draft, Writing – review & editing, Supervision. **Jialu Zheng:** Investigation, Writing – review & editing. **Xuelian Chen:** Methodology. **Can Sun:** Methodology. **Hao Jiang:** Investigation, Data curation. **Guangrong Li:** Data curation. **Xiaoyong Zhang:** Conceptualization, Writing – review & editing, Supervision.

Declaration of Competing Interest

The authors declare that they have no known competing financial interests or personal relationships that could have appeared to influence the work reported in this paper.

Acknowledgment

This work is also supported by State Key Laboratory for Mechanical Behavior of Materials. Research fundings from the Natural Science Foundation Research Project of Shaanxi Province (Nos. 2019JQ-286, 2019JQ-184 and 2021JQ-603) are greatly acknowledged by the authors.

Appendix A. Supporting information

Supplementary data associated with this article can be found in the online version at doi:10.1016/j.jallcom.2021.161300.

References

- [1] F. Ji, L. Wang, S. Pang, P. Gao, H. Xu, G. Xie, J. Zhang, G. Cui, A balanced cation exchange reaction toward highly uniform and pure phase $FA_{1-x}MA_xPb_3$ perovskite films, *J. Mater. Chem. A* 4 (2016) 14437–14443.
- [2] W. Kong, Z. Ye, Q. Zhen, B. Zhang, H. Wu, Characterization of an abnormal photoluminescence behavior upon crystal-phase transition of perovskite $CH_3NH_3PbI_3$, *Phys. Chem. Chem. Phys.* 17 (2015) 16405–16411.
- [3] X. Hao, F. Zabihi, H. Wang, Q. Zhang, M. Eslamian, Grain engineering by ultrasonic substrate vibration post-treatment of wet perovskite films for annealing-free, high performance, and stable perovskite solar cells, *Nanoscale* 10 (2018) 8526–8535.
- [4] Z. Chu, M. Yang, P. Schulz, D. Wu, X. Ma, E. Seifert, L. Sun, X. Li, K. Zhu, K. Lai, Impact of grain boundaries on efficiency and stability of organic-inorganic trihalide perovskites, *Nat. Commun.* 8 (2017) 2230.
- [5] S. Ranbir, S.R. Suranagi, S.J. Yang, C. Kilwon, Enhancing the power conversion efficiency of perovskite solar cells via the controlled growth of perovskite nanowires, *Nano Energy* 51 (2018) 192–198.
- [6] X. Song, W. Wang, P. Sun, W. Ma, Z.-K. Chen, Additive to regulate the perovskite crystal film growth in planar heterojunction solar cells, *Appl. Phys. Lett.* 106 (2015) 033901.
- [7] J.W. Lee, H.S. Kim, N.G. Park, Lewis acid-base adduct approach for high efficiency perovskite solar cells, *Acc. Chem. Res.* 49 (2016) 311–319.
- [8] W. Ke, G. Fang, J. Wang, P. Qin, H. Tao, H. Lei, Q. Liu, X. Dai, X. Zhao, Perovskite solar cell with an efficient TiO_2 compact film, *ACS Appl. Mater. Interfaces* 6 (2014) 15959–15965.
- [9] Z.S. Almutawah, S.C. Watthage, Z. Song, R.H. Ahanharnejhad, K.K. Subedi, N. Shrestha, A.B. Phillips, Y. Yan, R.J. Ellingson, M.J. Heben, Enhanced grain size and crystallinity in $CH_3NH_3PbI_3$ perovskite films by metal additives to the single-step solution fabrication process, *MRS Adv.* 3 (2018) 3237–3242.
- [10] G. Dawit, I.M. Asuo, B. Daniele, B. Matteo, K. Ibrahimia, S.G. Cloutier, R. Federico, N. Riad, Solvent-antisolvent ambient processed large grain size perovskite thin films for high-performance solar cells, *Sci. Rep.* 8 (2018) 12885.
- [11] Z.G. Xiao, Q.F. Dong, C. Bi, Y.C. Shao, Y.B. Yuan, J.S. Huang, Solvent annealing of perovskite-induced crystal growth for photovoltaic-device efficiency enhancement, *Adv. Mater.* 26 (2014) 6503–6509.
- [12] A.F. Akbulatov, V.M. Martynenko, L.A. Frolova, N.N. Dremova, I. Zhidkov, S.A. Tsarev, S.Y. Luchkin, E.Z. Kurmaev, S.M. Aldoshin, K.J. Stevenson, P.A. Troshin, Intrinsic thermal decomposition pathways of lead halide perovskites $APbX_3$, *Sol. Energy Mater. Sol. Cells* 213 (2020) 110559.
- [13] E. Calabrò, F. Matteocci, B. Paci, L. Cinà, L. Vesce, J. Barichello, A. Generosi, A. Reale, A. Di Carlo, Easy strategy to enhance thermal stability of planar PSCs by perovskite defect passivation and low-temperature carbon-based electrode, *ACS Appl. Mater. Interfaces* 12 (2020) 32536–32547.
- [14] G. Tumen-Ulzii, C. Qin, T. Matsushima, M.R. Leyden, U. Balijipalli, D. Klotz, C. Adachi, Understanding the degradation of Spiro-OMeTAD-based perovskite solar cells at high temperature, *Sol. RRL* 4 (2020) 2000305.
- [15] H. Xiong, G. DeLuca, U. Bach, L. Jiang, Q. Zhang, E. Reichmanis, Y. Qiu, Synergistic effect of N,N-dimethylformamide and hydrochloric acid on the growth of $MAPbI_3$ perovskite films for solar cells, *ACS Omega* 5 (2020) 32295–32304.
- [16] C. Yang, Y. Peng, T. Simon, T. Cui, Control of PbI_2 nucleation and crystallization: towards efficient perovskite solar cells based on vapor-assisted solution process, *Mater. Res. Express* 5 (2018) 045507.
- [17] M. Jung, S.G. Ji, G. Kim, S.I. Seok, Perovskite precursor solution chemistry: from fundamentals to photovoltaic applications, *Chem. Soc. Rev.* 48 (2019) 2011–2038.
- [18] Y. Li, X. Li, Q. Chu, H. Dong, J. Yao, Y. Zhou, G. Yang, Tuning nucleation sites to enable monolayer perovskite films for highly efficient perovskite solar cells, *Coatings* 8 (2018) 408.
- [19] C. Bi, Q. Wang, Y.C. Shao, Y.B. Yuan, Z.G. Xiao, J.S. Huang, Non-wetting surface-driven high-aspect-ratio crystalline grain growth for efficient hybrid perovskite solar cells, *Nat. Commun.* 6 (2015) 7747.
- [20] K. Yan, M. Long, T. Zhang, Z. Wei, H. Chen, S. Yang, J. Xu, Hybrid halide perovskite solar cell precursors: colloidal chemistry and coordination engineering behind device processing for high efficiency, *J. Am. Chem. Soc.* 137 (2015) 4460–4468.
- [21] B. Li, D. Binks, G.Z. Cao, J.J. Tian, Engineering halide perovskite crystals through precursor chemistry, *Small* 15 (2019) 1903613.
- [22] Y.M. Xie, B. Yu, C. Ma, X. Xu, Y. Cheng, S. Yuan, Z.K. Wang, H.T. Chandran, C.S. Lee, L.S. Liao, S.W. Tsang, Direct observation of cation-exchange in liquid-to-solid phase transformation in $FA_{1-x}MA_xPb_3$ based perovskite solar cells, *J. Mater. Chem. A* 6 (2018) 9081–9088.
- [23] Y. Li, B. Ding, G.J. Yang, C.J. Li, C.X. Li, Achieving the high phase purity of $CH_3NH_3PbI_3$ film by two-step solution processable crystal engineering, *J. Mater. Sci. Technol.* 34 (2018) 1405–1411.
- [24] F. Zhang, Z. Ma, T. Hu, R. Liu, Q. Wu, Y. Yu, H. Zhang, Z. Xiao, M. Zhang, W. Zhang, X. Chen, H. Yu, Ultra-smooth $CsPbI_2Br$ film via programmable crystallization process for high-efficiency inorganic perovskite solar cells, *J. Mater. Sci. Technol.* 66 (2021) 150–156.
- [25] H. Zhang, J. Zhuang, X. Liu, Z. Ma, H. Guo, R. Zheng, S. Zhao, F. Zhang, Z. Xiao, H. Wang, H. Li, Defect passivation strategy for inorganic $CsPbI_2Br$ perovskite solar cell with a high-efficiency of 16.77%, *J. Mater. Sci. Technol.* 82 (2021) 40–46.
- [26] X. Ye, H. Cai, J. Su, J. Yang, J. Ni, J. Li, J. Zhang, Preparation of hysteresis-free flexible perovskite solar cells via interfacial modification, *J. Mater. Sci. Technol.* 61 (2021) 213–220.
- [27] L. Meng, Q. Wei, Z. Yang, D. Yang, J. Feng, X. Ren, Y. Liu, S. Liu, Improved perovskite solar cell efficiency by tuning the colloidal size and free ion concentration in precursor solution using formic acid additive, *J. Energy Chem.* 41 (2020) 43–51.
- [28] B. Li, M.J. Li, C.B. Fei, G.Z. Cao, J.J. Tian, Colloidal engineering for monolayer $CH_3NH_3PbI_3$ films toward high performance perovskite solar cells, *J. Mater. Chem. A* 5 (2017) 24168–24177.
- [29] B. Ding, L. Gao, L. Liang, Q. Chu, X. Song, Y. Li, G. Yang, B. Fan, M. Wang, C. Li, C. Li, Facile and scalable fabrication of highly efficient lead iodide perovskite thin-film solar cells in air using gas pump method, *ACS Appl. Mater. Interfaces* 8 (2016) 20067–20073.
- [30] Q.Q. Chu, B. Ding, Y. Li, L. Gao, Q. Qiu, C.X. Li, C.J. Li, G.J. Yang, B. Fang, Fast drying boosted performance improvement of low-temperature paintable carbon-based perovskite solar cell, *ACS Sustain. Chem. Eng.* 5 (2017) 9758–9765.
- [31] R. Lamaestre, H. Bernas, Significance of lognormal nanocrystal size distributions, *Phys. Rev. B* 73 (2006) 125317.
- [32] D.R. Wight, I.D. Blenkinsop, W. Harding, B. Hamilton, Diffusion-limited lifetime in semiconductors, *Phys. Rev. B* 23 (1981) 5495–5510.
- [33] P. Ajev, S. Miasojedovas, S. Jurnas, A carrier density dependent diffusion coefficient, recombination rate and diffusion length in $MAPbI_3$ and $MAPbBr_3$ crystals measured under one- and two-photon excitations, *J. Mater. Chem. C* 8 (2020) 10290–10301.
- [34] A. Guerrero, G. Garcia-Belmonte, I. Mora-Sero, J. Bisquert, Y.S. Kang, T.J. Jacobsson, J.P. Correa-Baena, A. Hagfeldt, Properties of contact and bulk impedances in hybrid lead halide perovskite solar cells including inductive loop elements, *J. Phys. Chem. C* 102 (2016) 8023–8032.
- [35] A. Pockett, G.E. Eperon, T. Peltola, H.J. Snaith, A. Walker, L.M. Peter, P.J. Cameron, Characterization of planar lead halide perovskite solar cells by impedance spectroscopy, open-circuit photovoltage decay, and intensity-modulated photovoltage/photocurrent spectroscopy, *J. Phys. Chem. C* 119 (2015) 3456–3465.